Variation Segmentation Layer in Deep Learning Network for SPECT Images Lesion Segmentation

Mohd Akmal Masud[1,4], Mohd Zamani Ngali[2,*], Siti Amira Othman[1], Ishkrizat Taib[2], Kahar Osman[3], Salihatun Md Salleh[2], Ahmad Zahran Md. Khudzari[3], Nor Salita Ali[4]

[1] Faculty of Applied Sciences and Technology, Universiti Tun Hussein Onn Malaysia, 84600 Panchor, Johor, Malaysia
[2] Faculty of Manufacturing and Engineering, Universiti Tun Hussein Onn Malaysia, 86400 Batu Pahat, Johor, Malaysia
[3] Faculty of Biosciences and Medical Engineering, Universiti Teknologi Malaysia, 81310 Johor Bahru, Johor, Malaysia
[4] Nuclear Medicine Department, National Cancer Institute, 62250 Putrajaya, Malaysia

ARTICLE INFO	ABSTRACT
Article history: Received 29 March 2023 Received in revised form 13 July 2023 Accepted 3 October 2023 Available online 25 December 2023 *Keywords:* SPECT; automated diagnosis; image classification; deep learning; CNN	Functional imaging, particularly single photon emission computed tomography (SPECT) Iodine-131 (I131) ablation imaging, has gained recognition as a useful clinical tool for diagnosing, treating, assessing as well as avoiding a variety of disorders, which includes metastasis. However, SPECT imaging is conspicuously characterized by low resolution, high sensitivity, limited specificity, and a low signal-to-noise ratio. Our study presents a deep learning method using 3D U-Net model with three variation segmentation layers (i.e., pixel classification (PC) layer, dice pixel classification (DPC) layer, and focal loss (FL) layer) to determine which layers have high accuracy to auto-segmentatize lesions using SPECT I131 ablation imaging. Deep Designer Network Apps was used to develop a 3D U-Net Convolutional Neural Network (CNN). Our results show that the DPC layer is a highly accurate segmentation for multi geometry lesion, PC layer is only suitable for one type of geometry and FC layer is the worst of all three. Additionally, only DPC can automatically segmentize four spheres using NEMA Phantom. The proposed DPC layer provides fast and robust lesion segmentation for SPECT I131 ablation imaging and can be improved in terms of accuracy using large number of ground truth data set.

1. Introduction

Deep learning algorithms have become increasingly popular in the medical imaging field since 2018 [1,2]. Various algorithms and models have been introduced under Convolution Neural Networks (CNN) for volume segmentation. Among the popular models for image segmentation are the U-Net model and the mask region CNN model. The U-Net model has 40 layers with 41 connections among the layers. Using methods such as convolution, max pooling, and ReLU layer as an activation function, this model can segment and classify medical images in various fields [3]. For example, many studies have used U-Net model for lesion segmentation, especially on SPECT images with poor resolution [4,5]. Other than lesions, U-Net model is often used to segment organs at risk in magnetic resonance

* *Corresponding author.*
E-mail address: zamani@uthm.edu.my (Mohd Zamani Ngali)

imaging (MRI) as well as computed tomography (CT) scan [6-8]. The aim of using the U-Net model for lesions or organs segmentation is to reduce the time taken to determine a region of interest (ROI) and further reduce uncertainties on each ROI made [9].

However, several issues plague U-Net deep learning, including number of training data. For example, for organ segmentation, the U-Net CNN plateaued at 160 cases, while 1000 slice images are required to obtain at least 75% accuracy for lesion SPECT imaging [5,10]. In lesion segmentation, especially in SPECT images, majority of U-Net models only focused on dice similarity coefficient (DSC), accuracy, and precision [11,12].

Aside from that, the type of segmentation layer in the U-Net model used for lesion segmentation in the image at the end of the layer is scarcely discussed. Hence, this paper will focus on lesion volume calculation using 3D U-Net model for SPECT images using I131 as a radiotracer. This study will then compare results obtained from three types of segmentation layers namely PC layer, DPC layer, and FL classification layer.

For training data, the Whole Body Ablation I131 patient images will be scanned using the Philips BrightView XCT modality. In addition, the National Electrical Manufacturers Association (NEMA) phantom image with sphere volume will be used to compare the three-layer segmentation layers. MATLAB 2022a will be used as a tool for ground truth labeling process using segmenter apps, and deep network designer apps will be used to develop a 3D U-Net network with 40 layers and 41 connections.

2. Materials and Methods
2.1 Whole Body Ablation I131 SPECT Images

Whole Body Ablation I131 SPECT images were gathered in diagnosing differentiated thyroid carcinoma using Philips BrightView XCT imaging equipment at National Cancer Institute, Putrajaya. In performing a SPECT test, the equipment records the patient's intravenous administration of the radiotracer I131. Clinical metastases were found in 84 patients, with age ranging from 24 to 67. The said SPECT images may display the majority of a patient's body due to its size (130 (width) × 130 (height) × 90 (slices)). Additionally, a radiation dosage matrix was expressed by a 16-bit unsigned integer, and every bone SPECT image was kept in a DICOM file (.dcm). Therefore, SPECT images vary greatly from natural images, which have pixel values ranging from 0 to 255, due to the radiation's broad dosage range.

2.2 Data Preprocessing
2.2.1 Image normalization

In order to segment the data for this study, head-to-neck position was extracted from the data. After image normalization was done, image boundary is conducted to standardize each image size and bit depth (size = 130 × 130 × 36, bit depth = 8 grayscale) due to irregular data obtained after segmentation [13]. In addition, the image normalization procedure can increase the accuracy of image processing, leading to highly precise segmentation.

2.2.2 Data augmentation

For training, the model needs a lot of data to possess high generalization capabilities. There are well-known issues with SPECT nuclear medicine imaging including scarcity of raw data and high cost

of human labeling [14]. In order to increase the number of original data, this research employs four different augment types (i.e., rot90, fliplr, flipud, and rot90 (fliplr)) as data improvement techniques.

2.3 Image Cropping

In order to retrieve the head-to-neck region from 130 × 130 × 90 Whole Body Ablation I131 SPECT images, the head-to-neck cropping area tries to isolate the sections of the spine and ribs from the others. However, it is sometimes difficult to clearly distinguish between different body regions in noisy, low-resolution bone SPECT images. Additionally, conventional separation techniques are ineffective for Whole Body Ablation I131 SPECT imaging since they only consider skeleton structure information. Thus, radiation dosage distribution ought to be utilized to crop the thorax area dynamically. The transformation of 130 × 130 × 90 whole-body ablation I131 SPECT images into 130 × 130 × 36 whole-body ablation I131 SPECT images is shown in Figure 1.

2.4 SPECT Images Labelling

Images labeling is crucial in training a dependable deep learning-based segmentation model under the supervised learning domain. However, for SPECT images, the process is arduous and consumes more time given its low spatial resolution. Therefore, image segmenter apps in MATLAB 2022a were used to label the backgrounds and lesions in the head-to-neck area [12]. Labeled lesions are on the uptake of the thyroid gland, parotid gland, submandibular and sublingual gland. The diagnostic report (in text format) and head-to-neck SPECT image (in DICOM format) is imported into volume segmenter apps, as shown in Figure 1. In this study, default DICOM format values for brightness, contrast and threshold were used for lesion and background labeling (using the smallest paintbrush size in the toolbar).

All the SPECT images manual annotation findings are utilized as experiment ground truth (as a logical .mat file) to create a combined annotation file that is input into the segmentation models.
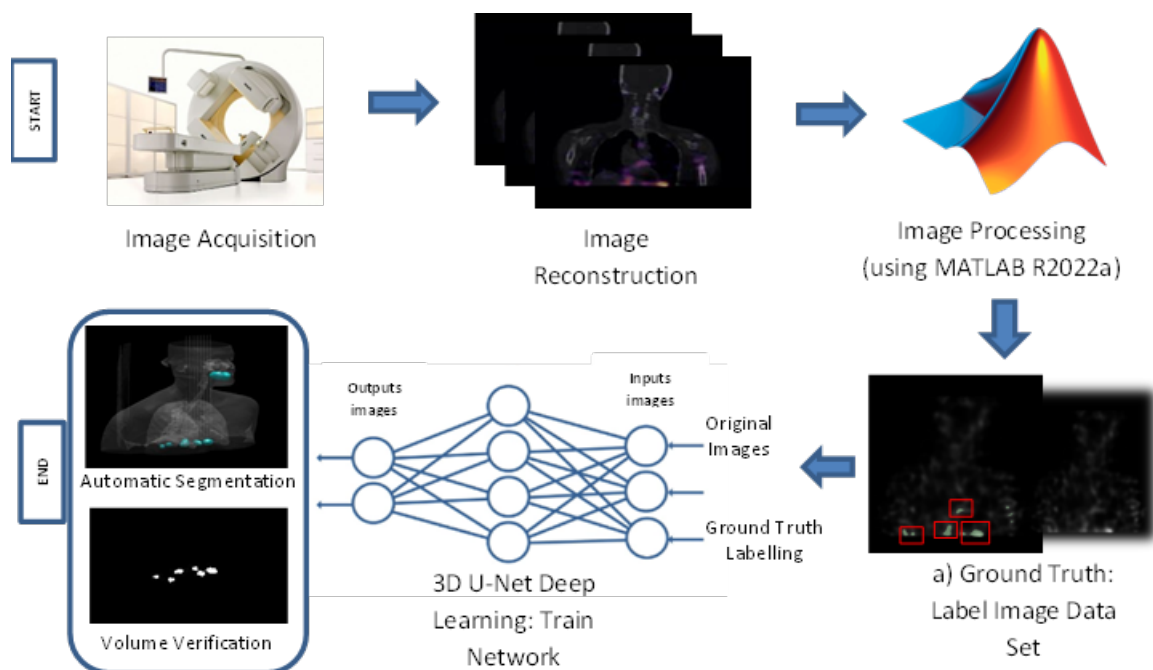

Fig. 1. Workflow for images labeling and training

2.5 Segmentation Models

This work discusses deep segmentation models based on the mainstream Convolution Neural Networks (CNN) developed using deep network designer apps in MATLAB 2022a [15]. 3D U-Net model was built using the layer library function in the deep learning toolbox. The process to design 3D U-Net includes a contraction path (e.g., downsampling) for recording context and an asymmetric expansion path (e.g., upsampling) for accurate localization, as shown in Figure 2.

(a) Contraction path: This approach adjusts for downsampling an imputed image via repeated application of two 3 × 3 convolutions, preceded by a ReLU and a 2 × 2 max pooling with stride 2. At each downsampling stage, the number of feature channels will be doubled.

(b) Expansion path: This entails an upsampling of the feature map, two 3 × 3 convolutions, each followed by a ReLU, a 2 × 2 convolution that cuts the number of feature channels in half, concatenation with the suitably cropped feature map from the contracting path. Segmentation layers consist of three different final layers namely PC layer, DPC layer, and FL layer.
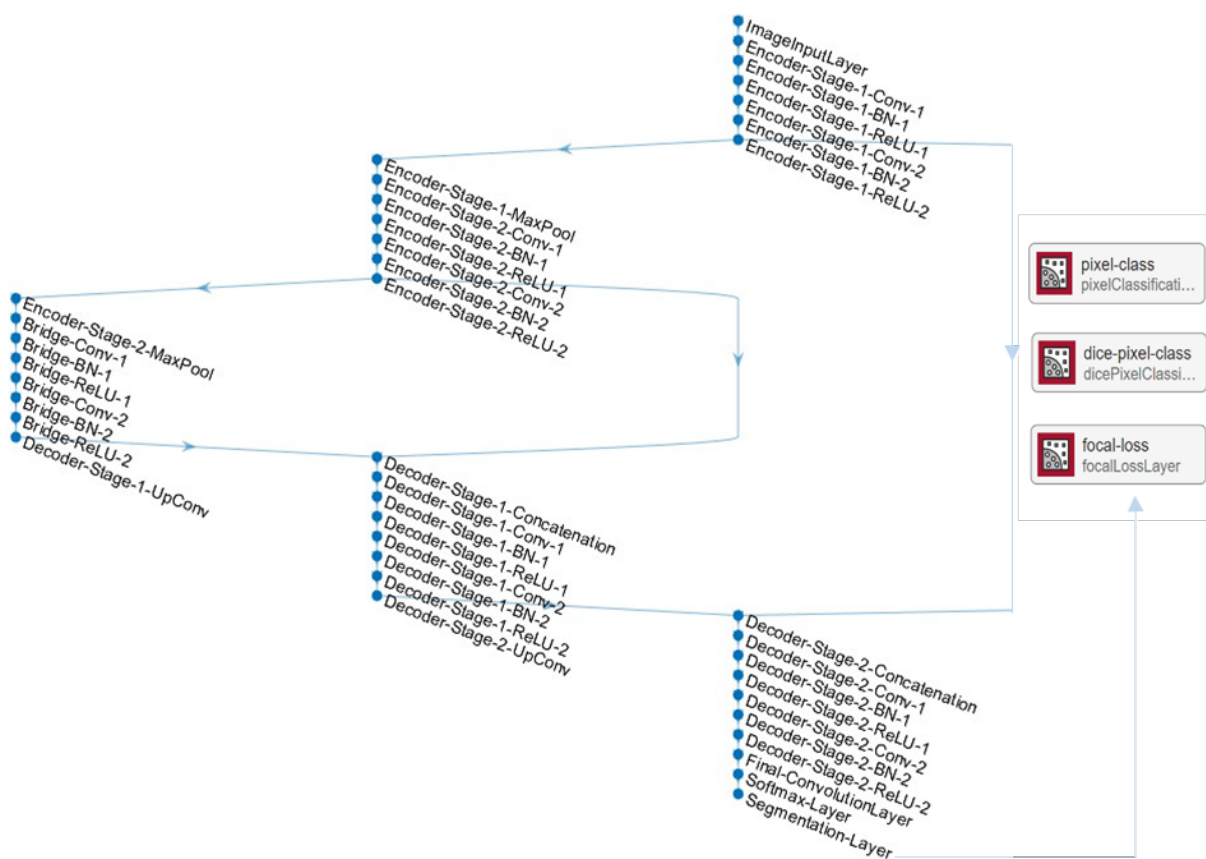

Fig. 2. 3D U-Net layers

2.6 Evaluation Index

Segmentation outcomes of the model are quantitatively assessed using metrics that are often employed in medical image segmentation. Intersection of Union (IoU), Dice Similarity Coefficient (DSC), and Root Mean Square Deviation (RMSD) are the corresponding evaluation metrics to determine the accuracy level [16-18].

The RMSD measures how much a particular molecular structure deviates from a reference geometry [19,20]. This method is suitable to be used to evaluate percentage difference of values for

different volume segmentations simultaneously. The RMSD indicates the quadratic mean of the differences between anticipated and observed values or the square root of the second sample moment of those disparities [21]. Formula for RMSD is as follows.

Eq. (1): Root Mean Square Deviation (RMSD)

$$\text{Root Mean Square Deviation (RMSD)} = \sqrt{\sum((Pi - Oi)2 / n}) \tag{1}$$

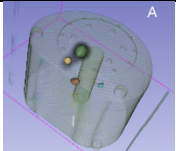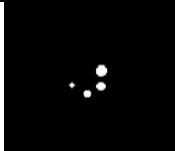Eq. (2): Intersection of Union (IoU)

$$IoU = \frac{TP}{TP+FP+FN}. \tag{2}$$
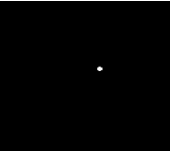
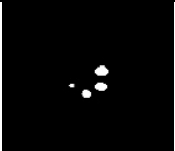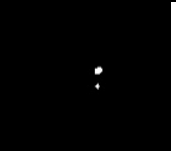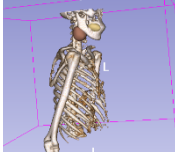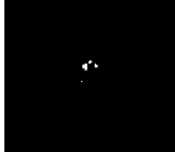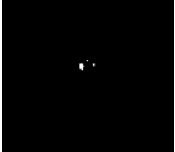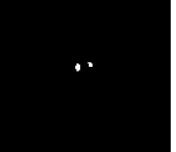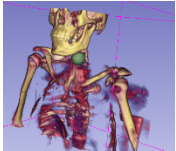Eq. (3): Dice Similarity Coefficient (DSC)

$$Dice\ Similarity = \frac{2*TP}{2*TP+(FP+FN)}. \tag{3}$$

3. Result

Three data sets were used in this study, namely; 1) NEMA phantom with six spheres insert, 2) Set 1 Gland: Thyroid, Parotid, Submandibular, Sublingual, 3) Set 2 Gland: Thyroid only. Note that these sets were tested using three different segmentation layers: PC layer, DPC layer, and FL layer. In Table 1, column 2 is the fusion of a SPECT image and a CT image; column 3 shows the ground truth labeling image for the training data set; finally, columns 4, 5, and 6 are the auto-segmentation images for three different segmentation layers.

Table 1
Data set for ground truth image labeling

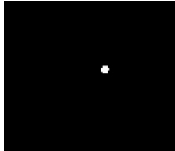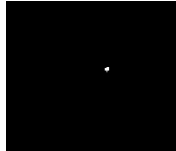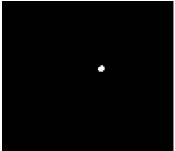| Data Set	Original Images	Ground Truth Labelling	PC Layer	DPC Layer	FL Layer
NEMA Phantom					
Set 1 Gland: Thyroid, Parotid, Submandibular, Sublingual					
Set 2 Gland: Thyroid only					

Based on Table 2, the NEMA phantom with six spheres insert was evaluated using RMSD, IoU as well as DSC via three different types of segmentation layers. The results show that RMSD for DPC layer gave the highest accuracy (23.98) compared to PC layer (27.16) and FL layer (42.54). However, for DSC and IoU, the PC layer recorded the highest accuracy with 0.8035 and 0.6716, respectively.

Table 2 shows that only the DPC layer can segment all four spheres, while the PC layer and FL layer can only segment three. It can be observed here that although the DPC layer can segment four spheres, the DSC and IoU are slightly lower compared to the PC layer, which is 0.7706 and 0.6269, respectively. This is the same finding as Zhang *et al.,* [22], and Taha and Hanbury [23], where the authors found that lowest RMSD value does not necessarily corresponds to the best method. Instead, DSC and IoU needs to be considered in determining the most accurate method.

Table 2

Comparison of experimental results of three segmentation layers for NEMA phantom data set

NEMA Phantom

Evaluation/Segmentation Layer	No. of Sphere	Actual Volume (ml)	Calculated Volume (ml)	Root Mean Square Deviation (RMSD)	Dice Similarity Coefficient (DSC)	IoU
PC	1	26.52	18.7	27.16	0.8035	0.6716
	2	11.5	9.7			
	3	5.57	4.1			
	4	2.57	0.0			
DPC	1	26.52	24.4	23.98	0.7706	0.6269
	2	11.5	16.3			
	3	5.57	10.2			
	4	2.57	2.0			
FL	1	26.52	13.1	42.54	0.4983	0.3319
	2	11.5	2.3			
	3	5.57	0.0			
	4	2.57	0.0			

For patients image data set, labeling lesions are only taken from the head to the thorax area to test segmentation of the thyroid gland, parotid gland, submandibular gland and sublingual gland in a training data set in determining which segmentation layer has the highest accuracy. For example, patient 1 is a metastasis patient, where all the uptake is in all the four glands. Meanwhile, patient 2 only has uptake in the thyroid gland.

Table 3 exhibits that the DPC layer has high accuracy for RMSD, DSC, and IoU for patient 1, which are 28.51, 0.7940, and 0.6585, respectively. Meanwhile, the PC layer for patient 1 recorded the lowest accuracy for RMSD, DSC, and IoU, which are 45.01, 0.4690, and 0.3063, correspondingly. Consequently, the DPC layer recorded the lowest accuracy for patient 2, at 92.31, 58.07, and 0.0421 for RMSD, DSC, and IoU. This is because in the patient training data set, the ground truth labeling on thyroid gland uptake is limited: only 27 sets of patients data images were compared with the ground truth labeling set on the parotid gland, submandibular gland, and sublingual gland uptake. Note that this contradicts results discovered by Park *et al.,* [24].

Table 3
Comparison of experimental results of three segmentation layers for set 1 gland data set

Set 1 Gland: Thyroid, Parotid, Submandibular, Sublingual						
Evaluation/Segmentation Layer	Patient No.	Actual Volume (ml)	Calculated Volume (ml)	Root Mean Square Deviation (RMSD)	Dice Similarity (DSC)	Intersection of Union (IoU)
PC	1	22.2	4.17	45.01	0.4690	0.3063
		6.2	3.79			
	2	9.54	1.91	79.97	0.3333	0.2000
DPC	1	22.2	15.5	28.51	0.7940	0.6585
		6.2	3.2			
	2	9.54	4.0	58.07	0.0808	0.0421
FL	1	22.2	5.5	38.3	0.6330	0.4591
		6.2	5.3			
	2	9.54	4.6	51.7	0.6524	0.4842

For Table 4, only patients with uptake in the thyroid gland are labeled and trained to see if there is significant use of the DPC layer for RMSD, DSC, and IoU compared to the training data in Table 3. The results show that RMSD, DSC, and IoU recorded the highest accuracy for the DPC layer, which are 42.34, 0.7333, and 0.5789. However, values for the PC layer for RMSD, DSC, and IoU are much lower compared to the DPC layer, which are 84.27, 0.2727, and 0.1579. Meanwhile, results for the FL layer are 57.02, 0.6029, and 0.4316 for RMSD, DSC, and IoU, respectively.

The DPC layer has the highest accuracy because all the labeled thyroid glands seem to have the same shape for the labeling data. Thus, when the labeling data is trained, accuracy of the data reaches its maximum level at a low iteration, which is at the 20th iteration. Meanwhile, the PC layer produces the lowest accuracy due to inconsistency in the labeled pixel value. This means that if any labeled data has a high difference between one data and another, the efficiency of data learning is relatively low compared to training data with many labeled pixels and consistency.

Table 4
Comparison of experimental results of three segmentation layers for set 2 gland data set

Set 2 Gland: Thyroid Only						
Evaluation/Segmentation Layer	Patient No.	Actual Volume (ml)	Calculated Volume (ml)	Root Mean Square Deviation (RMSD)	Dice Similarity (DSC)	Intersection of Union (IoU)
PC	1	9.54	1.5	84.27	0.2727	0.1579
DPC	1	9.54	5.5	42.34	0.7333	0.5789
FL	1	9.54	4.1	57.02	0.6029	0.4316

Figure 3 illustrates the training data graph for the three sets of images: NEMA phantom, Set 1 Gland, and Set 2 Gland. From the said figure, it can be observed that when using the DPC layer on training data with different forms of ground truth labeling, the graph loss will slow down for stable conditions as shown in Figure 3(e). Figure 3(d) notes that the loss decreases at the 120th iteration. This is quite different from the PC layer in Figure 3(b), where the loss decreases starting from the 30th iteration. This suggests that the network system is not able to quickly learn a data set involving different shapes if it uses DPC as a segmentation layer.
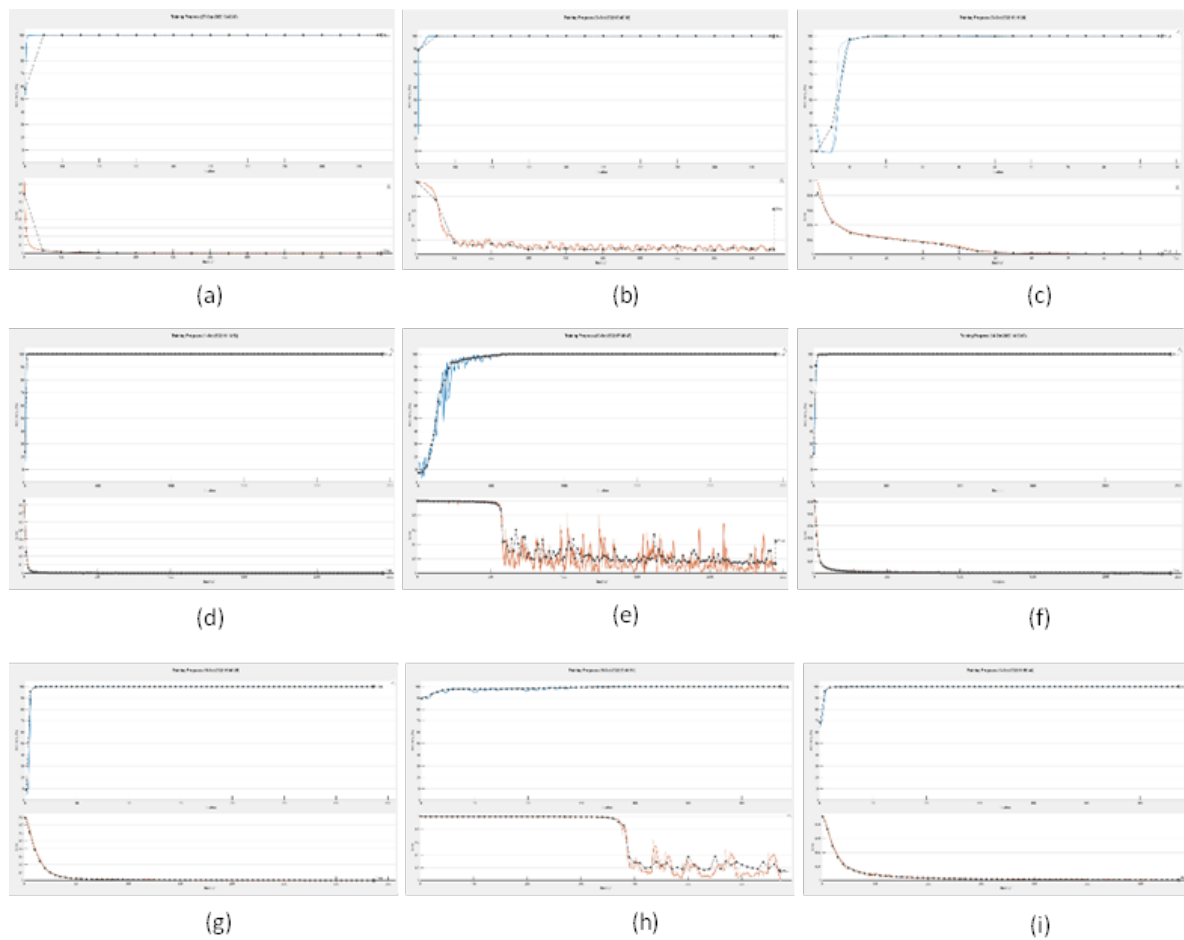
Fig. 3. Graph training for accuracy and loss: (a) NEMA Phantom PC Layer Training Graph, (b) NEMA Phantom DPC Layer Training Graph, (c) NEMA Phantom FL Layer Training Graph, (d) Set 1 Gland PC Layer Training Graph, (e) Set 1 Gland DPC Layer Training Graph, (f) Set 1 Gland FL Layer Training Graph, (g) Set 2 Gland PC Layer Training Graph, (h) Set 2 Gland DPC Layer Training Graph, (i) Set 2 Gland FL Layer Training Graph

For PC layer, the loss decreases at the 30th iteration because the training data sets used have the same pixel range. This causes the 3D U-Net model took only a short duration to reach maximum accuracy. This is similar to results obtained by Bardis *et al.,* [10], Zhang *et al.,* [22], Mürschberger *et al.,* [25], Ashok and Gupta [26], which found that for huge data set, time taken for the loss graph to decrease horizontally and obtain higher accuracy shortens. In the study, the author stated that dice similarity has high accuracy in the training data set of 160 cases.

For Set 1 Gland, the image used is quite complicated because when the ground truth labeling is made, the uptakes in the parotid gland, submandibular gland, and sublingual gland seem connected. This makes the labeling ground truth shaped, connects the three glands, and causes all evaluations (RMSD, DSC, and IoU) to record high accuracies. In addition, this study found that DPC layer is suitable to train data that have various uptake ground truth labeling shapes and pixel sizes.

4. Conclusion

This study found that different types of segmentation layer provide different segmentation volumes for the same data on 3D U-Net network. In this paper, three types of segmentation layer namely PC layer, DPC layer and FL layer were proposed for three batches of images data. The main contribution of this work is in developing the 3D U-Net network using deep network designer apps

and labeling the ground truth using volume segmenter in MATLAB software. One of the issues faced by this study is the difficulty to determine the exact threshold pixel value in every lesion due to no solid artifact reference (e.g., CT image). Results of this study found that the choice of segmentation layer should be based on the types of data set used. In specific, DPC layer is only suitable for one form of ground truth labeling (e.g., to segment the liver). In contrast, the PC layer is only suitable to be used on a large data set, thus, SPECT images are suitable to be implemented using the PC layer because they have various lesion shapes. On the other hand, the FL layer shows insufficient data for all three sets. For future research, the proposed method should be compared with attention mechanism function and layer augmentation to obtain the best result.

Acknowledgment

References

[1] Namdev, Utkarsh, Shikha Agrawal, and Rajeev Pandey. "Object Detection Techniques based on Deep Learning: A Review." *Computer Science & Engineering: An International Journal (CSEIJ)* 12, no. 1 (2022): 125-134. https://doi.org/10.5121/cseij.2022.12113

[2] Abdolali, Fatemeh, Jeevesh Kapur, Jacob L. Jaremko, Michelle Noga, Abhilash R. Hareendranathan, and Kumaradevan Punithakumar. "Automated thyroid nodule detection from ultrasound imaging using deep convolutional neural networks." *Computers in Biology and Medicine* 122 (2020): 103871. https://doi.org/10.1016/j.compbiomed.2020.103871

[3] Livne, Michelle, Jana Rieger, Orhun Utku Aydin, Abdel Aziz Taha, Ela Marie Akay, Tabea Kossen, Jan Sobesky et al. "A U-Net deep learning framework for high performance vessel segmentation in patients with cerebrovascular disease." *Frontiers in Neuroscience* 13 (2019): 97. https://doi.org/10.3389/fnins.2019.00097

[4] Papandrianos, Nikolaos, Elpiniki Papageorgiou, Athanasios Anagnostis, and Konstantinos Papageorgiou. "Bone metastasis classification using whole body images from prostate cancer patients based on convolutional neural networks application." *PloS One* 15, no. 8 (2020): e0237213. https://doi.org/10.1371/journal.pone.0237213

[5] Lin, Qiang, Chuangui Cao, Tongtong Li, Zhengxing Man, Yongchun Cao, and Haijun Wang. "dSPIC: a deep SPECT image classification network for automated multi-disease, multi-lesion diagnosis." *BMC Medical Imaging* 21, no. 1 (2021): 1-16. https://doi.org/10.1186/s12880-021-00653-w

[6] Li, XiuHua, ShuiCheng Zhu, LiMing Song, ShiQi Wang, and QiQiang Liang. "Algorithm for Segmentation of Liver Tumor Based on Improved U-Net Model." In *2021 International Conference on Electronic Information Engineering and Computer Science (EIECS)*, pp. 346-349. IEEE, 2021. https://doi.org/10.1109/EIECS53707.2021.9588057

[7] Li, Xiaomeng, Hao Chen, Xiaojuan Qi, Qi Dou, Chi-Wing Fu, and Pheng-Ann Heng. "H-DenseUNet: hybrid densely connected UNet for liver and tumor segmentation from CT volumes." *IEEE Transactions on Medical Imaging* 37, no. 12 (2018): 2663-2674. https://doi.org/10.1109/TMI.2018.2845918

[8] Zhang, Jingyi, Mengge Huang, Tao Deng, Yongchun Cao, and Qiang Lin. "Bone metastasis segmentation based on Improved U-NET algorithm." In *Journal of Physics: Conference Series*, vol. 1848, no. 1, p. 012027. IOP Publishing, 2021. https://doi.org/10.1088/1742-6596/1848/1/012027

[9] Che, Guoyi, Yongchun Cao, Ao Zhu, Qiang Lin, Zhengxing Man, and Haijun Wang. "Segmentation of bone metastases based on attention mechanism." In *2021 IEEE International Conference on Power Electronics, Computer Applications (ICPECA)*, pp. 259-263. IEEE, 2021. https://doi.org/10.1109/ICPECA51329.2021.9362531

[10] Bardis, Michelle, Roozbeh Houshyar, Chanon Chantaduly, Alexander Ushinsky, Justin Glavis-Bloom, Madeleine Shaver, Daniel Chow, Edward Uchio, and Peter Chang. "Deep learning with limited data: Organ segmentation performance by U-Net." *Electronics* 9, no. 8 (2020): 1199. https://doi.org/10.3390/electronics9081199

[11] Liu, Liangxia, Yongchun Cao, Qiang Lin, Zhengxing Man, and Weiqiong Wang. "Multi-disease classification of whole-body scintigraphy images based on deep learning." In *2022 7th International Conference on Intelligent Computing and Signal Processing (ICSP)*, pp. 133-137. IEEE, 2022. https://doi.org/10.1109/ICSP54964.2022.9778791

[12] Zhao, Shaofang, Xiaoyan Chen, and Qang Lin. "Classifying SPECT Bone Metastasis Images in Grayscale Format with

VGGNets." In *2021 International Conference on Communications, Information System and Computer Engineering (CISCE)*, pp. 409-414. IEEE, 2021. https://doi.org/10.1109/CISCE52179.2021.9446029

[13] Seaman, M. "Cryofluorescence Tomography (CFT) is an Ex Vivo Tool to Study Anatomy, Physiology, and Drug or Tracer Distribution in Brain and Other Organs." *Molecular Imaging Biology* 18, no. Suppl 1 (2016): S1554-S1859.

[14] Lin, Qiang, Mingyang Luo, Ruiting Gao, Tongtong Li, Zhengxing Man, Yongchun Cao, and Haijun Wang. "Deep learning based automatic segmentation of metastasis hotspots in thorax bone SPECT images." *PLoS One* 15, no. 12 (2020): e0243253. https://doi.org/10.1371/journal.pone.0243253

[15] Kulkarni, Arun D. "Deep Convolution Neural Networks for Image Classification." *International Journal of Advanced Computer Science and Applications* 13, no. 6 (2022): 18-23. https://doi.org/10.14569/IJACSA.2022.0130603

[16] Husin, Akmal Hakim, Syahmil Hakim Hamzani, Shahrin Hisham Amirnordin, Mohd Faizal Mohideen Batcha, Rafiuddin Wahidon, and Makatar Wae-hayee. "Drying Studies of Oil Palm Decanter Cake for Production of Green Fertilizer." *Journal of Advanced Research in Fluid Mechanics and Thermal Sciences* 97, no. 2 (2022): 66-79. https://doi.org/10.37934/arfmts.97.2.6679

[17] Toulkeridou, Evropi, Carlos Enrique Gutierrez, Daniel Baum, Kenji Doya, and Evan P. Economo. "*Automated segmentation of insect anatomy from micro-CT images using deep learning*." bioRxiv (2021). https://doi.org/10.1101/2021.05.29.446283

[18] Zhou, Zongwei, Md Mahfuzur Rahman Siddiquee, Nima Tajbakhsh, and Jianming Liang. "Unet++: A nested u-net architecture for medical image segmentation." In *Deep Learning in Medical Image Analysis and Multimodal Learning for Clinical Decision Support: 4th International Workshop, DLMIA 2018, and 8th International Workshop, ML-CDS 2018, Held in Conjunction with MICCAI 2018, Granada, Spain*, September 20, 2018, Proceedings 4, pp. 3-11. Springer International Publishing, 2018. https://doi.org/10.1007/978-3-030-00889-5_1

[19] Zavorin, Alexander S., Lyudmila L. Lyubimova, Konstantin V. Buvakov, Roman N. Fisenko, Alexander A. Tashlykov, and Alexander I. Artamontsev. "Root-mean-square deviations of atomic positions-nanoscale indicator of surface condition." *Bulletin of the Tomsk Polytechnic University, Geo Assets Engineering* 331, no. 11 (2020): 37-47.

[20] Finocchiaro, Domenico, Salvatore Berenato, Elisa Grassi, Valentina Bertolini, Gastone Castellani, Nico Lanconelli, Annibale Versari, Emiliano Spezi, Mauro Iori, and Federica Fioroni. "Partial volume effect of SPECT images in PRRT with 177Lu labelled somatostatin analogues: a practical solution." *Physica Medica* 57 (2019): 153-159. https://doi.org/10.1016/j.ejmp.2018.12.029

[21] Sabooding, Rusmadee, Juntakan Taweekun, and Mas Fawzi. "Analysis of Aerosol Optical Depth for Thailand, Malaysia and Singapore from Satellite and Sunphotometer during 2011-2017." *Journal of Advanced Research in Fluid Mechanics and Thermal Sciences* 53, no. 1 (2019): 47-52.

[22] Zhang, Junqian, Yingming Sun, Hongen Liao, Jian Zhu, and Yuan Zhang. "Automatic parotid gland segmentation in MVCT using deep convolutional neural networks." *ACM Transactions on Computing for Healthcare (HEALTH)* 3, no. 2 (2021): 1-15. https://doi.org/10.1145/3485278

[23] Taha, Abdel Aziz, and Allan Hanbury. "Metrics for evaluating 3D medical image segmentation: analysis, selection, and tool." *BMC Medical Imaging* 15, no. 1 (2015): 1-28. https://doi.org/10.1186/s12880-015-0068-x

[24] Park, Junyoung, Jae Sung Lee, Dongkyu Oh, Hyun Gee Ryoo, Jeong Hee Han, and Won Woo Lee. "Quantitative salivary gland SPECT/CT using deep convolutional neural networks." *Scientific Reports* 11, no. 1 (2021): 7842. https://doi.org/10.1038/s41598-021-87497-0

[25] Mürschberger, Nina, Maximilian P. Reymann, Philipp Ritt, Torsten Kuwert, A. Hans Vija, Michal Cachovan, and Andreas Maier. "U-Net for Multi-Organ Segmentation of SPECT Projection Data." In *2020 IEEE Nuclear Science Symposium and Medical Imaging Conference (NSS/MIC)*, pp. 1-2. IEEE, 2020. https://doi.org/10.1109/NSS/MIC42677.2020.9507779

[26] Ashok, Malvika, and Abhishek Gupta. "Deep learning-based techniques for the automatic segmentation of organs in thoracic computed tomography images: A Comparative study." In *2021 International Conference on Artificial Intelligence and Smart Systems (ICAIS)*, pp. 198-202. IEEE, 2021. https://doi.org/10.1109/ICAIS50930.2021.9396016